Journal of
Synchrotron Radiation

ISSN 0909-0495

Received 5 March 2009
Accepted 11 December 2009

Microcrystallography using single-bounce monocapillary optics

R. E. Gillilan,[a]* M. J. Cook,[a] S. W. Cornaby[b,c]‡ and D. H. Bilderback[b,a]

[a]MacCHESS (Macromolecular Diffraction Facility at CHESS), Ithaca, NY, USA, [b]School of Applied and Engineering Physics, Cornell University, Ithaca, NY, USA, and [c]CHESS (Cornell High-Energy Synchrotron Source), Cornell University, Ithaca, NY, USA. E-mail: reg8@cornell.edu

X-ray microbeams have become increasingly valuable in protein crystallography. A number of synchrotron beamlines worldwide have adapted to handling smaller and more challenging samples by providing a combination of high-precision sample-positioning hardware, special visible-light optics for sample visualization, and small-diameter X-ray beams with low background scatter. Most commonly, X-ray microbeams with diameters ranging from 50 μm to 1 μm are produced by Kirkpatrick and Baez mirrors in combination with defining apertures and scatter guards. A simple alternative based on single-bounce glass monocapillary X-ray optics is presented. The basic capillary design considerations are discussed and a practical and robust implementation that capitalizes on existing beamline hardware is presented. A design for mounting the capillary is presented which eliminates parasitic scattering and reduces deformations of the optic to a degree suitable for use on next-generation X-ray sources. Comparison of diffraction data statistics for microcrystals using microbeam and conventional aperture-collimated beam shows that capillary-focused beam can deliver significant improvement. Statistics also confirm that the annular beam profile produced by the capillary optic does not impact data quality in an observable way. Examples are given of new structures recently solved using this technology. Single-bounce monocapillary optics can offer an attractive alternative for retrofitting existing beamlines for microcrystallography.

Keywords: microbeam single-bounce capillary optics.

1. Introduction

For a uniformly illuminated sample, the number of photons per diffraction spot, as given by Darwin's formula (Darwin, 1914*a*,*b*; Woolfson, 1970), is proportional to the volume of the crystal. This unfortunate fact means that the total number of diffracted photons from a sample decreases as the cube of the linear sample dimension. The task of improving diffraction for the smallest of samples requires more than simply increasing the incident flux or exposure time (Glaeser *et al.*, 2000). Because crystals are typically suspended in fluid when mounted, excess fluid can produce unwanted background scatter when X-ray beams are larger than the diameter of the crystal. X-ray microbeams offer a significant advantage in that they concentrate photons where they are most needed: on the sample rather than the supporting matrix. Besides background reduction, small beams also provide a means of selectively exposing portions of larger crystals in the hope of finding better diffraction (Cusack *et al.*, 1998; Sanishvili *et al.*, 2008). Not only do protein crystals frequently exhibit imperfections in growth, they often grow in clusters, bundles of needles, stepped sheets, and other conglomerations that make single-crystal isolation difficult. Indeed, the use of X-ray microfocus optics for locating well ordered regions in otherwise poor crystals may be one of the most important applications of X-ray microbeams in protein crystallography.

X-ray microbeams have been in use for some time and a variety of strategies have been employed for their generation at synchrotrons: Kirkpatrick and Baez (KB) mirrors (Kirkpatrick & Baez, 1948; Mimura *et al.*, 2007), single-bounce monocapillary (Balaic *et al.*, 1995), multi-bounce monocapillary (Bilderback *et al.*, 1994), polycapillary optics (Li & Bi, 1998), Fresnel zone plates (Yun *et al.*, 1992) and compound refractive lenses (Snigirev *et al.*, 1996). Emerging technologies such as waveguides (Pfeiffer *et al.*, 2002; Feng *et al.*, 1995; Lagomarsino *et al.*, 1996), Laue and kinoform lenses also offer promising new opportunities (Kang *et al.*, 2006; Evans-Lutterodt *et al.*, 2003; Aristov *et al.*, 2000). Recently, microbeams have become more widely available to the protein crystallography community, owing in large part to the dis-

‡ Present affiliation: Moxtek Inc., Orem, UT, USA.

semination of technology developed at ESRF ID13 (Riekel, 2004; Riekel *et al.*, 2005). The majority of currently operating microdiffraction beamlines employ highly developed KB mirror technology which is commercially available. Beam diameters of the order of tens to hundreds of nanometers have been achieved with these methods.

We present an alternative for retrofitting existing synchrotron beamlines for a microbeam based on single-bounce capillary optics. Optics fabricated from capillaries possess a number of useful characteristics: they are potentially inexpensive to produce and are mechanically robust and radiation resistant. Being achromatic, a single optic can function over a wide range of energies (up to 80 keV) and range of bandwidths without change in spot position, spot size or beam divergence. High demagnification can be achieved using a capillary with a very short focal length. Capillary optics are compact, do not require a cumbersome vacuum environment, combine both horizontal and vertical focusing in a single element, and can be aligned using pre-existing optical table mechanisms. In fact, capillary optic housings resemble aperture-based collimators and can be easily interchanged.

In this paper we outline the overall design of the microbeam components used at MacCHESS, and discuss the mounting hardware, stability and alignment procedures employed. We examine background scattering, beam profile and its effect on diffraction spots and processing statistics. Diffraction statistics obtained using a capillary microbeam are significantly better than those obtained using standard collimated beam when sample size, crystal quality and mounting technique are the same.

At large sample-to-detector distances, the monocapillary optics produce a distinct beam profile in the Bragg reflections. Comparison of these reflections at various sample-to-detector distances reveals that the beam profile does not produce an observable negative effect large enough to outweigh the background reduction that happens naturally with increasing detector distance. Finally, we review several recent uses of our capillary microbeam optics in solving new protein structures.

2. Capillary design

Without any special surface treatment or coating, glass is capable of greater than 95% reflectivity at shallow (grazing incidence) angles; consequently the internal surface of a tapered glass capillary can act as an efficient focusing optic for X-rays (Stern *et al.*, 1988). Capillaries can be used in either single- or multiple-bounce mode. Bundles of multi-bounce capillaries (polycapillaries) have been used successfully for protein crystallography on laboratory sources, where their ability to collect X-rays from wide angles and large sources is an advantage (Li & Bi, 1998). In this paper we concentrate on single-bounce monocapillaries, since their characteristics are better suited to crystallography on synchrotron sources.

Balaic *et al.* were the first to use a capillary with a parabolic internal profile to obtain protein crystal diffraction patterns (Balaic *et al.*, 1995). Subsequently, parabolic capillaries have been used on laboratory sources to solve several unknown structures (Hrmova *et al.*, 2001; Varghese *et al.*, 2002). Parabolic profiles assume a source at infinite distance from the focal spot. For sources at finite distances, particularly when additional upstream focusing elements are present, elliptical profiles are more precise, though differences are slight for typical beamline configurations. Production of capillaries with elliptical profiles was first described by Bilderback & Fontes (1997). Ongoing engineering advances now allow for the routine production of optics with internal elliptical profiles that are well suited for use in many protein crystallography applications at synchrotron sources (Huang & Bilderback, 2006; Cornaby, 2008) (see also http://glasscalc.chess.cornell.edu/Cornaby_Capillary_Handbook_2008.pdf).

X-rays entering the wider upstream end of a capillary are reflected by the internal walls to a focal spot some distance beyond the tip (Fig. 1). When illuminating the full inside surface of the capillary, unfocused beam will normally pass directly through the center opening. This beam may or may not be problematic for the experiment, depending upon factors like beam diameter, divergence and focal length. In any event, it can be removed by use of a round upstream beamstop or appropriately placed slits if necessary.

Several groups have used ray-tracing techniques to evaluate potential capillary designs (Vincze *et al.*, 1998; Furuta *et al.*, 1993; Wang *et al.*, 1996; Thiel, 1998; Chen *et al.*, 1994; Vincze & Riekel, 2003). Huang & Bilderback have developed a practical analytical approach to designing capillaries that requires relatively few input parameters (Huang & Bilderback, 2001). The method has been implemented as a web-based capillary design calculator available online at http://glasscalc.chess.cornell.edu/ImageProf.html. Horizontal and vertical source size (full width at half-maximum, FWHM) and distance from source to optic are the key parameters characterizing the X-ray source. This is true even when slits and upstream focusing are present since they simply alter the effective size and distance parameters (Huang & Bilderback, 2004).

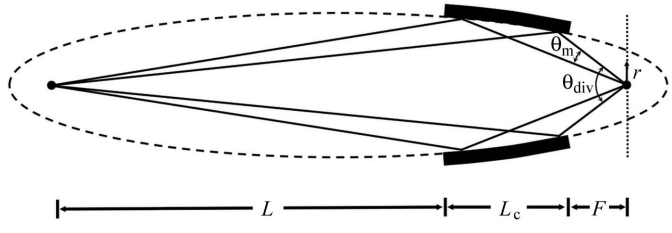

Figure 1
Cross-sectional view of a capillary segment with elliptical internal profile. X-rays from a divergent point source located at the left focus of the ellipse converge to the opposite (right) focus after reflecting at a glancing angle from the internal surface. The maximum divergence of the focused beam, $\theta_{\rm div}$, results from rays collected from opposite sides of the tube. A second smaller divergence, $\theta_{\rm m}$, is from the elliptical curvature itself. Focal length F, capillary length $L_{\rm c}$ and distance to source L, together with maximum divergence, fully specify the capillary design. Parameter r measures the radial distance from the center of the focal spot within the focal plane (dotted line). The scale is highly compressed for the purposes of illustration since $L \gg F$.

Maximum divergence, $\theta_{\rm div}$, focal length, F, and capillary length, $L_{\rm c}$, are the key input parameters describing the capillary itself (Fig. 1). The maximum divergence produced by a capillary is determined by the angle at the focal point subtended by the inside diameter of the tip. This value is limited only by the maximum grazing incidence angle permissible in glass: $\theta_{\rm div}/4 = \theta_{\rm grazing} = 0.2^\circ$ for 10 keV X-rays (Cornaby, 2008). But there is another divergence value associated with the capillary. While rays reflecting off opposite sides of the tube converge with angle $\theta_{\rm div}$, rays reflecting from the same side converge with angle $\theta_{\rm m} < \theta_{\rm div}/2$ (Fig. 1). By limiting how much of the internal capillary surface is illuminated, the maximum divergence of the focused beam can be varied. In this mode, the optic can function much like a classical ellipsoidal condensing mirror with separate meridional and sagittal curvatures (Howell & Horowitz, 1975; Cornaby *et al.*, 2008). In the present work we will consider only full capillary illumination with unblocked direct beam at a synchrotron source; consequently, $\theta_{\rm div}$ is the operative divergence to consider.

Beam divergence can contribute to spot overlap in diffraction images, particularly in the case of large unit cells. Synchrotron beamlines are highly desirable because of the narrow beam divergence (typically from as small as 0.1 mrad vertically to as large as 2–3 mrad horizontally). Laboratory sources typically have beam divergence in the range 1–2 mrad (Yang *et al.*, 1999), though state-of-the-art microfocus systems can run above 4 mrad (MicroMax-007 HF microfocus, Rigaku).

The degree of demagnification of the source by a capillary can be estimated as $M = F/L$, the ratio of focal length to distance from source (Fig. 1; Cornaby, 2008). The capillary gain as a function of radial distance, r, from the spot center on the focal plane is obtained by integrating flux along the length of the capillary, t (Huang & Bilderback, 2006),

$$G(r) = \frac{y_0^2}{F^2(\delta^2/L^2 + \alpha^2)} \int_{1/(1+L_{\rm R})}^{1} \exp\left[-\left(r^2/r_0^2\right)t^2\right] {\rm d}t. \quad (1)$$

For simplicity, we use the formula given for a round source of width δ. The integration range is determined by $L_{\rm R} \equiv L_{\rm c}/F$, the capillary length relative to the focal distance. The radius of the capillary tip opening y_0 is related to maximum divergence: $2y_0/F \simeq \theta_{\rm div}$; consequently, either increasing divergence or decreasing focal length increases gain. Both source width δ and angle of average slope error α act to reduce the overall gain. The width of the distribution defined by the integral in (1) is determined by

$$r_0 = F\left(\delta^2/L^2 + \alpha^2\right)^{1/2}. \quad (2)$$

The focal spot size is thus limited by both source width and slope error and decreases linearly with focal length. When $\delta^2/L^2 > \alpha^2$, size is dominated by source divergence alone and the capillary slope errors become insignificant.

The maximum gain at the center of the focal spot,

$$G(0) = \frac{y_0^2}{F^2(\delta^2/L^2 + \alpha^2)} \frac{L_{\rm R}}{(1 + L_{\rm R})}, \quad (3)$$

increases linearly with $L_{\rm R}$ for short capillaries, but approaches a point of diminishing returns for $L_{\rm R} > 2$. While longer capillaries collect more overall flux, less flux is concentrated at the center, so the profile sharpness has declined. Formulae incorporating more realistic flat-source parameters also show this trend (Huang & Bilderback, 2006).

In the case studied here, upstream focusing by standard beamline optics already produces a significant gain in the beam delivered to the capillary; consequently optimal capillary designs need only produce additional gains in the range of ten to a few hundred. The F1 station at CHESS uses horizontal and vertical focusing mirrors at 7.1 m and 4.4 m from the sample, respectively, to achieve a 1.4 mm × 0.2 mm focal spot with 1.0 mrad × 0.4 mrad divergence. An effective source can be defined at the 4.4 m mirror position by projecting backwards from the focal spot using the known divergence. Assuming therefore an 80 µm × 80 µm capillary entrance, we can compute a back-projected source size at 4400 mm. Let s be a source width with divergence θ. The size a distance l away from the source is given by $[s^2 + (\theta l)^2]^{1/2}$: 4.6 mm × 1.8 mm (Cornaby, 2008). While the analytical formulas for gain are most accurate for distant sources, they can still provide useful estimates for closer secondary sources. Our 50 mm capillary with 22 mm focal distance (enough to leave room for a cryostream) and 2.0 mrad maximum divergence yields a predicted 20 µm secondary focal spot with five- to six-fold gain. A variety of capillaries have been drawn to these specifications and tested on F1 with gains ranging from 11 to 17 and spot diameters ranging from 12 to 20 µm. More accurate gain and profile calculations on secondary sources require numerical treatment of the angular dependency of the source profile or full ray-tracing (Huang & Bilderback, 2004; Barrea *et al.*, 2009).

We have assumed a slope error of 50 µrad. The spot size is limited by the source divergence in this case, so from (2) the only option for decreasing spot size is to decrease the focal distance at the expense of either divergence or total flux (by further limiting the entrance size). A 50 µm × 50 µm source, for example, can achieve a 1 µm focal spot with ×1200 gain if the slope errors are below 25 µrad with the divergence and capillary length parameters defined above.

The nanoscale smoothness of pulled glass is quite good, about 2–3 nm r.m.s., and is not considered to be a limiting factor in achieving small focal spots on currently available synchrotron sources (Cornaby, 2008). Of greater importance are deviations from ideal surface shape introduced during the drawing process. Current drawing technology has reduced observed slope errors (measured at the external capillary surface) to below 30 µrad with profile deviations of order 1 µm r.m.s. This places the theoretical minimum focal spot size close to 1 µm for a typical capillary configuration (Huang & Bilderback, 2006). Micrometer beams have recently been tested for protein crystallography by several groups, but are not yet routinely available (Moukhametzianov *et al.*, 2008).

By carefully illuminating small patches on an internal capillary surface, researchers at ESRF were recently able to locate a region of low slope error that allowed them to achieve focal spots down to 250 nm (Snigirev *et al.*, 2007). The present optical quality of single-bounce monocapillaries is thus more than adequate for focal spot sizes currently of use to protein crystallographers (5–20 μm) and they offer potential for even smaller spot sizes in next-generation synchrotron sources.

3. Mounting, stability and alignment

While capillary optics are usually fabricated from comparatively thick-walled glass tubing, the very high tolerance requirements for the shape of the optic suggest that even modest deformations, such as strain induced by mounting hardware or even sag owing to weight, may be important. For reference, currently at CHESS a deviation of the order of 5 μm along a 10 cm-long optic will destroy the focusing of the optic, and a deviation of the order of 1 μm may affect the focal spot size. Computational estimates based on the theory of flexure for simple beams do indeed indicate that deformations of the order of 0.35 μm are possible in cases of inadequate mounting for the capillary examined here. Much larger deviations for capillaries of greater length or thinner glass are possible since sag increases as the square of the length. Details of the computation are presented in Appendix *A*. Fig. 2 compares the deformation of a capillary 5 cm in length owing to gravity when supported at the end points with that of a capillary supported so as to minimize the figure error. Supports are indicated in the figure as triangles. Capillary supports optimized for minimum slope error are almost identical (not shown). Optimal supports in this case fall roughly at 1/4 and 3/4 positions along the tube. While positional errors introduced by the drawing process currently stand at around 1 μm, optimal support placement is clearly essential for the production of higher-precision optics necessary at small-source-size facilities, particularly those expected at next-generation synchrotron sources.

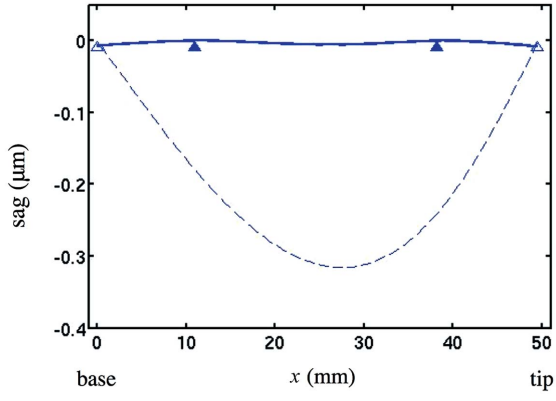

Figure 2
Distortion of the capillary figure owing to gravity. Calculations from the theory of flexure of simple beams (Appendix *A*) show that proper mounting is an important factor if capillary figure errors are to be reduced to a level appropriate for next-generation X-ray sources. The *y*-axis represents deviations from the ideal centerline of the optic. Support points are shown as triangles, with open triangles corresponding to the dashed line. The solid line supported at the solid triangles represents an optimally supported optic which minimizes overall figure error.

Design of the mounting hardware is shown in cross section in Fig. 3(*a*). Discs for supporting the capillary are mounted within a precision-bored reamed barrel. The holes in each disc through which the capillary is mounted are bored to a diameter designed to match the capillary outside diameter at the specified support positions to within 0.5 thousandths of an inch (12 μm). Each hole was partially countersunk to minimize the actual contact surface area.

A positioner block with aperture slightly smaller than the upstream outside diameter of the capillary pushes the optic gently in place and doubles as an upstream aperture limiting stray scatter into the glass. Vitron O-rings are used to apply gentle pressure to the positioner and capillary. A special motorized mount has been designed that allows for precise optimization of sample-to-optic distance (Fig. 3*b*). For beams diverging at 2 mrad and less, errors that might result from manual positioning are not significant compared with the size of the beam: a 1 mm error in the sample-to-optic distance, for example, would increase a 20 μm focal spot by only 2 μm. A visual registration mark on the outside barrel corresponding to the front end of the capillary facilitates manual positioning. For smaller focal spot sizes and more divergent beams, the motorized sample-to-optic distance is more critical. Also, the ability to retract the optic reproducibly away from the sample is useful during manual sample mounting.

Both slits and aperture-based collimators produce some parasitic background scatter that must be removed using either guard slits or guard apertures. Capillary optics are based

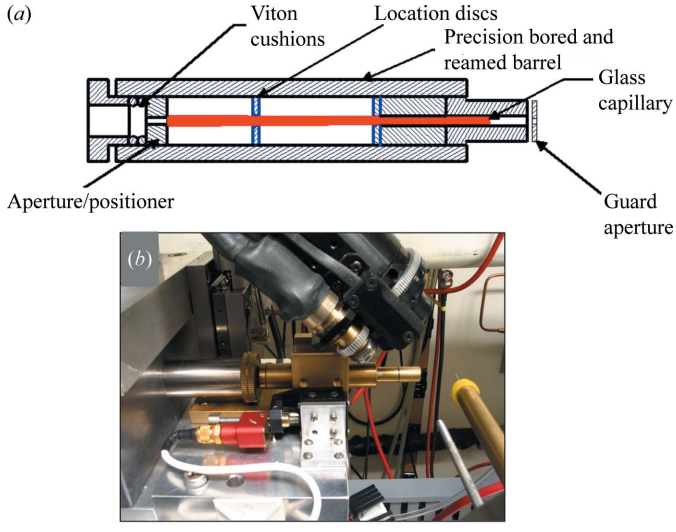

Figure 3
Design and mounting of capillary optics. A precision-bored barrel (*a*) encloses the glass capillary, which is supported by two location discs of precisely defined aperture. Gentle pressure is applied using a plug with viton cushions to hold the optic in place. A guard aperture to remove parasitic scatter is positioned at the end of the enclosure about 10 mm from the tip of the capillary. The barrel is mounted on a movable base (*b*) controlled with a piezomotor (red in the lower left) from New Focus, San Jose. A black registration mark on the end of the barrel (right) marks the tip of the capillary and is used for manual positioning. The sample is mounted on the yellow plastic base at the far right.

Table 1
Diffraction data statistics for 18 μm capillary microfocus and 100 μm collimated beam on similar proteinase K crystals.

	100 μm beam (13.510 keV)		Capillary microbeam (13.510 keV)			
Crystal size (μm)	40 × 30 × 30	25 × 20 × 20	35 × 25 × 25	35 × 30 × 40	40 × 35 × 20	30 × 30 × 25
Resolution range (Å)	50.0–1.80	50.0–2.10	50.0–1.80	50.0–1.63	50.0–1.52	50.0–1.53
Highest shell (Å)	1.86–1.80	2.18–2.10	1.86–1.80	1.69–1.63	1.57–1.52	1.58–1.53
Unique reflections	22795	14589	23019	30801	37797	37149
Rejected (%)	0.11	0.04	0.04	0.02	0.03	0.03
$R_{\rm merge}$ (%)†	0.191	0.139	0.175	0.147	0.123	0.119
Multiplicity	3.8	3.5	3.8	3.7	3.5	3.5
Completeness (%)	99.9	99.3	99.5	92.5	99.2	94.9
χ^2‡	0.79	0.68	0.70	0.71	0.74	0.70
$\langle I/\sigma\rangle$ overall	7.97	5.89	8.79	9.83	10.73	10.68
$\langle I/\sigma\rangle$ highest shell	(2.24)	(2.15)	(2.40)	(2.08)	(2.20)	(2.41)
Mosaicity	0.15–0.18	0.27–0.31	0.16–0.21	0.25–0.28	0.17–0.21	0.20–0.23
Unit cell						
a (Å)	67.78	67.87	67.99	67.99	67.99	67.99
b (Å)	67.78	67.87	67.99	67.99	67.99	67.99
c (Å)	102.20	102.33	102.40	102.52	102.46	102.55

† Total linear *R*-merge reported by *HKL2000* ($\Sigma|I_{\rm obs} - I_{\rm avg}|/\Sigma I_{\rm avg}$). ‡ *Scalepack* normalized goodness-of-fit index $[\Sigma(I - \langle I\rangle)^2/\sigma^2]$.

on specular reflection of X-rays from glass at very shallow angles, and the glass can be a source of parasitic scatter, including Compton scattering, X-ray fluorescence from trace elements, and small-angle scatter from the tip and the base of the optic. A guard aperture can be placed after the optic to eliminate most of the parasitic scattering from the glass (Engstrom & Riekel, 1996). The capillary housing design permits placement of a guard aperture 10 mm from the end of the capillary, leaving 12 mm of working distance to the sample (Fig. 3*a*). A quantitative assessment of parasitic scattering is given in §2 of the supplementary material for this paper.[1]

As with all focusing optics, capillaries require precise alignment. This task can be accomplished using pre-existing optical table mechanisms that are commonly used for aperture-based collimators. Total flux is not, at present, a sufficiently sensitive diagnostic for automated alignment. Currently, we use a far-field direct-beam imaging camera in combination with scintillating glass microfibers. The procedure should be effective down to nanometer-sized beams. Details are given in Appendix *B*.

4. Comparison with aperture-collimated beam

While the various advantages of microbeam in protein crystallography have been demonstrated elsewhere in the literature (Sanishvili *et al.*, 2008), detailed comparisons of single-bounce monocapillary optics with regular non-microfocused collimation at synchrotron sources have not been examined. The increased rate of radiation damage for focused beam makes a direct comparison of focused and collimated beam on the same crystal problematic when a complete dataset is required. To control for variation among crystals, we harvested multiple microcrystals of approximately the same dimensions from the same hanging drop. Proteinase K (EMD Chemicals, 70663-4, batch number D00041045) was treated with the inhibitor phenylmethylsulfonyl fluoride, PMSF (Sigma-Aldrich P7626, lot number 068K0726), and made up to a 24 mg ml^{-1} concentration in 100 m*M* HEPES buffer at pH 7.0. Well solutions containing 2 *M* $(NH_4)_2SO_4$, 25% PEG 4000, and 100 m*M* sodium acetate at pH 4.6 produced abundant octahedral microcrystals by the hanging-drop method. These crystals were larger in diameter than the 18 μm capillary beam, but smaller than the 100 μm standard collimator. All samples were mounted using mineral oil in 75 μm-diameter micromounts (MiTeGen, Ithaca, NY, USA). While proteinase K crystals grow as almost regular octahedra, size estimates are quoted as maximum visible dimensions on the calibrated beamline microscope optics when the sample mount is viewed direct and edge-on (see Table 1). The microscope optics have a resolving power of about 2.5 μm, therefore crystal dimensions given are accurate to within ±2.5 μm. Though these crystals are not particularly small by current standards, they represent a commonly encountered size and, being just smaller than the conventional 100 μm-diameter beam, are the largest crystals for which a significant gain using microbeam should be expected purely on the basis of size.

Both the standard collimation and microbeam exposures were taken on CHESS beamline F1 contiguously at a wavelength of 0.918 Å (13.51 keV). All exposures were 20 s and 90° of data were collected for each crystal. With $P4_32_12$ symmetry, the datasets were all greater than 93% complete with at least 3.5-fold multiplicity. Thus, 93% of the possible Bragg reflections were collected at the specified resolution, and each reflection was observed an average of 3.5 times owing to symmetry. The maximum resolution of each dataset is reported as the *d*-spacing [$\lambda/2\sin(\theta)$ with scattering angle 2θ] at which $\langle I\rangle/\langle\sigma\rangle > 2$ [from *Scalepack* output (Otwinowski & Minor, 1997)]. Final $\langle I/\sigma\rangle$ values are reported as calculated by the CCP4 program *Truncate* (French & Wilson, 1978). The χ^2 statistic, also reported by *Scalepack*, is an additional indicator of quality in the error estimates (Borek *et al.*, 2003).

Resolutions obtained with the microbeam were consistently higher than those obtained with the 100 μm collimated beam by about 0.3 Å. Detailed statistics are given in Table 1. Mosaic

[1] Supplementary data for this paper are available from the IUCr electronic archives (Reference: BF5024). Services for accessing these data are described at the back of the journal.

spread is a beam-independent indicator of crystal quality (as long as beam divergence is small by comparison). Crystals with higher mosaic spreads tend to have lower resolution for both beam types; nonetheless, comparisons between samples of comparable mosaicity show significant advantage for microbeam. While resolution cut-offs have been chosen so that signal-to-noise estimates are comparable for all samples in the highest-resolution shells, overall $\langle I/\sigma \rangle$ values show a significant improvement for monocapillary microbeam. Overall $R_{\rm merge}$ statistics all appear to be better. Favourably, unit-cell parameters also show less variability for microbeam than for regular beam. This may be a result of the fact that microbeam samples a smaller and possibly more uniform portion of the crystal than macrobeam.

5. Beam and spot profiles

Normal aperture-based collimation selects a 100 µm circular region from the (primary) focal spot. The capillary optics examined here, which are used in place of collimation, collect an 80 µm circular patch of photons from the primary focus to produce a secondary focus at the sample. The beam intensity profile in the focal plane for the capillary optic has been measured and compared with geometric optics calculations (Huang & Bilderback, 2004). Total flux through the optic (CHESS F1) has been measured at 2.8×10^{10} photons s^{-1} which corresponds to an average of 1.1×10^{8} photons s^{-1} μm^{-2}.

As noted earlier, the beam at the sample consists of two components, a 40 µm FWHM direct beam converging with 0.45 mrad and a brighter 20 µm FWHM beam converging with 2 mrad. The two profile widths are close enough that the direct beam is essentially lost in the base of the focused beam and does little to influence the overall shape of the profile. At large distances downstream of the focal plane, the focused radiation spreads out to form an annulus around the less divergent direct beam. This pattern, while very useful for alignment purposes, may potentially result in unusual diffraction spot shapes at large detector-to-sample distances.

Diffraction spot profiles are influenced by a number of factors in addition to the incident beam profile: the detector point spread function, the angle of incidence of the beam on the detector surface, crystal mosaicity, cracks and multiple lattices, streaks from diffuse scattering, and even overall crystal shape. To evaluate the possible effect of spot shapes on diffraction patterns, we have collected diffraction data on a single large lysozyme crystal through a range of sample-to-detector distances. While a sample-to-detector distance of 180 mm would typically be used for a crystal of this quality, a range of larger distances are examined here in order to amplify possible beam profile effects. To control for the systematic effects of radiation damage, we alternated between long and short detector distances, minimizing overall dose by using 1 s exposures on a large ($\sim 100 \times 100 \times 100$ µm) crystal. At each of nine distances ranging from 136 mm to 876 mm, 20 exposures were taken over the same 10° wedge of data ($\Delta\varphi = 0.5°$) and scaled together using *Scalepack*.

Spots falling closest to the beamstop strike the detector surface almost perpendicular and result in the least geometric distortion to the visible profile. Fig. 4 shows the spot profile for reflection (−2 −2 1) at 18.8 Å over a range of distances represented both as surface plots and as pixels. The image contrast has been chosen to enhance the visibility of the annular region for the pixel images and the surface plots have been scaled to the same height for easy comparison. In actuality, the peak height of the 136 mm result is six times taller than the 876 mm result. Only beyond about 500 mm distance is the annular region visibly distinguishable from the central peak.

The diffraction datasets from 136 mm to 718 mm were each independently indexed and scaled using *HKL2000* over a resolution range of 20–4.6 Å as set by the longest distance used (718 mm). In this way, each set of statistics represents approximately the same set of low-order diffraction spots. The 872 mm dataset was omitted because it was judged to restrict the overall comparison to too few reflections. While the necessarily low average redundancy of these datasets introduces some uncertainty into the linear *R*-factors, it can be seen in Table 2 that there is actually a systematic trend of improvement in the terms with increasing distance. This increase in *R*-factor occurs despite a slight increasing trend in the number of unique reflections, which would normally work against improvement of the *R*-factor. The average signal-to-noise values reported in Table 2, $\langle I/\sigma \rangle$, are calculated from the

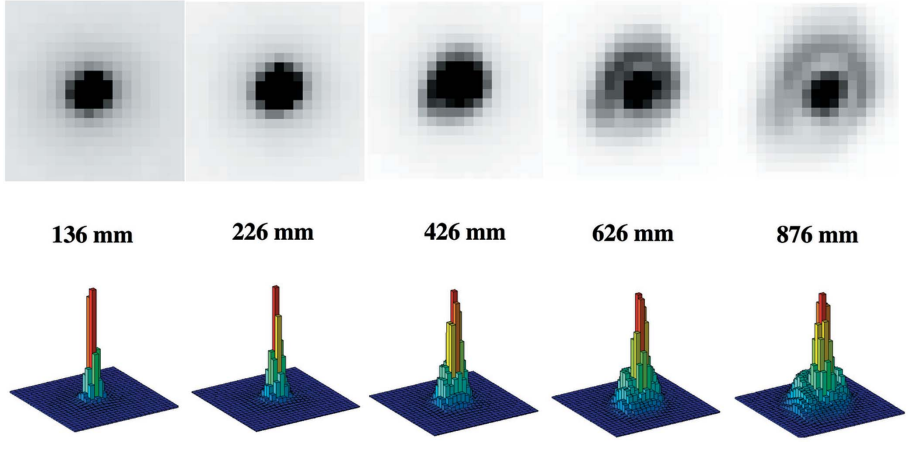

Figure 4
Diffraction spot profile as a function of detector distance. Diffraction spots close to the beamstop begin to show the characteristic annular microbeam profile once the sample-to-detector distance exceeds about 500 mm. This (−2 −2 1) reflection, which occurs at 18.8 Å, was produced by a large 100 µm-diameter good-quality lysozyme crystal. The upper row of images has been contrast-enhanced to make the halo visible. The lower row of surface plots has been scaled to uniform height for easy comparison. In actuality, the 136 mm profile is six times taller than the 876 mm profile.

Table 2
Effect of sample-to-detector distance on diffraction data statistics for a single large lysozyme crystal†.

Distance (mm)	Unique reflections	Redundancy	Linear R	$\langle I/\sigma\rangle$‡	χ^2§
135.7	267	1.4	0.090	7.89	1.3
168.4	280	1.4	0.089	8.17	1.3
222.8	286	1.4	0.080	8.85	1.3
320.9	295	1.5	0.074	9.36	1.3
418.5	298	1.5	0.077	9.40	1.4
516.0	298	1.5	0.072	9.34	1.2
614.0	293	1.5	0.059	10.35	1.2
718.0	356	1.0	0.063	9.09	1.0

† All data were collected on the same 10° wedge in the range 20–4.6 Å using 20 0.5° steps with 1 s exposures. ‡ Computed using the CCP4 *Truncate* program using *Scalepack* results. § Reported by *Scalepack* based on error parameters typically ranging from 0.09 to 0.12.

Scalepack output *via* the *Truncate* program (French & Wilson, 1978). They also show a systematically improving trend with distance.

These somewhat surprising results may be understood in the following way. Bragg reflections from an ideal crystal reflect the highly collimated nature of the synchrotron source (including optics), while diffuse scattering (such as that from disordered solvent) constitutes a more divergent source with photons being distributed along a wide range of angles. Air absorption plays only a minor role here by reducing overall intensity without contributing to background. Air scattering is constant in these experiments because the beamstop remained at a fixed distance from the sample. While the decrease of background in relation to Bragg reflections with detector distance has been observed and commented upon in the literature (Dauter, 1999; Pflugrath, 1999), a rigorous description is difficult owing to the heterogeneous and complex nature of background scattering. In principle, a very broad reflection should give rise to a noisier signal since the photons are spread among a larger number of detector pixels. Further, mis-shapen spots could potentially lead to integration or profile problems. Apparently for this modestly divergent beam, neither of these two negative factors is significant in comparison with the reduction in background scatter gained at larger distances.

6. Conclusions

Single-bounce monocapillary X-ray optics are a relatively easy and effective means of retrofitting existing synchrotron beamlines for protein microcrystallography. While the current slope and figure errors introduced during fabrication have yet to reach the low levels enjoyed by KB mirrors and other established optics, single-bounce monocapillaries do have a number of unique and potentially useful features, particularly as secondary focusing elements. An online design program facilitates customization of the optics to both application and source. A mounting scheme has been implemented which minimizes distortion of the optic, reduces parasitic scattering, and maintains design tolerances appropriate for next-generation sources. The system is mechanically robust and allows beamline personnel to change between conventional collimation and microbeam optics with relative ease.

Resolution limits in protein crystal diffraction obtained using capillary microbeam are consistently better than those using standard aperture-based collimation for the proteinase K microcrystals examined here. The $R_{\rm merge}$ statistics and overall average signal-to-noise ratio ($\langle I/\sigma\rangle$) are also better. While general improvements in data quality for microcrystals are to be expected when using microbeam, our data demonstrate that the unique nature of this capillary microbeam optic with its unusual spot profile does not significantly impact the quality of the data. In particular, a series of diffraction datasets taken on one large lysozyme crystal at various sample-to-detector distances reveals an improvement in signal-to-noise ratio in spite of unusual spot profiles at large distances.

Single-bounce monocapillary microfocus X-ray beams at MacCHESS have proven advantageous in a number of recent studies in structural biology. Crystals of a zinc transport protein which formed serendipitously during a BioSAXS experiment were harvested on site and the structure solved using MAD techniques in combination with microbeam data collection methods (Cherezov *et al.*, 2008; Höfer *et al.*, 2007). One of two 3 µm-thick plates discovered in the bottom of a dried sample tube containing a new serinocyclin from *Metarhizium anisopliae* yielded a complete microbeam dataset solvable by *ab initio* methods (Krasnoff *et al.*, 2007). Capillary microbeam data collected at MacCHESS have also been used by Ferguson *et al.* (Schmiedel *et al.*, 2008; Schmitz *et al.*, 2008) and by Ke *et al.* (Lu *et al.*, 2008). X-ray microbeam using single-bounce monocapillary optics is currently available upon request at all MacCHESS beamlines.

APPENDIX *A*
Capillary distortion (sag) under gravity

To estimate the degree of distortion a capillary optic will experience owing to its own weight, we can invoke the theory of flexure for simple beams (Eshbach, 1975). For a capillary of length L aligned along the x axis, let $D(x)$ represent the perpendicular distance from the x axis to the internal reflecting surface of the capillary. Divide the capillary into N short segments, each with center x_i and length ΔL. The weight on each segment, acting along the y axis (vertical), is given by

$$w_i = (\pi/4)\Delta L g \rho\left(\mathrm{OR}_i^2 - \mathrm{IR}_i^2\right), \tag{4}$$

where g is the acceleration due to gravity and ρ is the density of the glass. Owing to conservation of fluid volume during the drawing process, the ratio of outside radius OR_i to inside radius IR_i at any point along x is expected to be a constant, χ, so that $\mathrm{IR}_i = D(x_i)$ and $\mathrm{OR}_i = \chi \mathrm{IR}_i$.

The bending of a small section of an elastic beam under a load is given by

$$\frac{1}{R_i} = \frac{M_i}{E I_i}, \tag{5}$$

in which R_i is the radius of curvature at x_i and E is Young's elastic modulus that relates stress to strain in the material

(glass). The second moment of area, I, for a small section of the capillary is the y^2-weighted integral over the cross-sectional area,

$$I = \int y^2 \, \mathrm{d}A = \frac{\pi}{64}\left(\mathrm{OR}^4 - \mathrm{IR}^4\right). \quad (6)$$

A simple beam is supported at the left and right points NL and NR, with $x_1 \leq \mathrm{NL} < \mathrm{NR} \leq x_N$. The bending moment, M_i, is the total torque on either side of the point x_i, taking into account the opposing reactions of the supports, R_L and R_R,

$$M(x_i) = \sum_{j=2}^{i} -w_j(x_i - x_j) + \begin{cases} 0 & x_i \leq \mathrm{NL}, \\ R_\mathrm{L}(x_i - \mathrm{NL}) & \mathrm{NL} < x_i < \mathrm{NR}, \\ R_\mathrm{L}(x_i - \mathrm{NL}) + R_\mathrm{R}(x_i - \mathrm{NR}) & \mathrm{NR} < x_i. \end{cases} \quad (7)$$

The torque on one side of x_i must balance the torque on the other side in all cases since the capillary is assumed to be stably supported. The reaction forces are given by equating the opposing torques at either support,

$$R_\mathrm{R} = \frac{1}{\mathrm{NR} - \mathrm{NL}} \sum_{i=1}^{N} w_i(x_i - N_\mathrm{L}) = R_\mathrm{L}. \quad (8)$$

Since $1/R \simeq \mathrm{d}^2y/\mathrm{d}x^2$ in the limit of small displacements, equation (5) can be numerically integrated to yield the displacement, $y(x)$, of the capillary under gravity. This leaves two constants of integration. Since we are interested in comparing the deformation of the capillary relative to an undistorted shape which spans the supports, we can choose $y(\mathrm{NL}) = 0$. While any constant can be added to the slope of $y(x)$ and still have it satisfy equation (5), the physically realistic choice is to satisfy the condition that the support points are level and hence the average slope between the supports is zero,

$$\sum_{\mathrm{NL}}^{\mathrm{NR}} \frac{\mathrm{d}y}{\mathrm{d}x} = y(\mathrm{NR}) - y(\mathrm{NL}) = 0. \quad (9)$$

A Fortran version of this algorithm was tested on a hollow quartz fiber, 52.3 cm in length with an inside diameter of 183 µm and an outside diameter of 290 µm (Fiberware: Berlin, Germany). The fiber was supported at its endpoints and manual measurements accurate to 0.3 mm were made of the displacement owing to sag. Predictions agreed to approximately 3%. More detailed tests were also performed on a tapered leaded glass tube, 57 cm in length with diameter varying from 966 µm down to 262 µm along its length. Supports were placed at various positions along the tube. Results show excellent agreement within expected experimental errors (see supplementary material).

For the calculations performed here, we have used the same computed capillary profile that was used to produce the actual optic (FC05) currently in use at MacCHESS. We assume an X-ray source of 2.0 mm × 0.2 mm FWHM located 25 m from the capillary. The capillary is 50.0 mm in length with a desired focal distance of 22.0 mm from the tip and a target divergence of 2.0 mrad at full illumination. The capillary inside diameter runs from 80 µm at the base to 44 µm at the tip. The borosilicate glass (type 7740) has an elastic modulus of $E = 6.8 \times 10^4$ N mm^{-2} and a density of $\rho = 2.23$ (Shand, 1958). The average ratio of outside to inside diameter is $\chi = 18.41$. The profile was calculated using the algorithm of Huang & Bilderback (2006) available through a publicly accessible webserver (http://glasscalc.chess.cornell.edu/ImageProf.html).

APPENDIX *B*
Alignment and far-field beam visualization

Since the capillary optics used in this paper are rotationally symmetrical about the central axis, only four degrees of freedom are required to fully align them with the X-ray beam: two translations and two rotations. For more divergent beams than we consider here, an additional motorized sample-to-capillary adjustment is necessary to place the sample accurately at the focal spot. While specialized mounting stages have been designed for developmental work at arbitrary stations (Cornaby, 2008), MacCHESS optical tables are already equipped with the necessary table motions needed to align standard aperture-based collimators. For simple aperture-based collimation, automatic alignment based on systematic scans of table orientation and position is very effective at maximizing flux, as long as some flux is initially present. The relationship between flux and capillary orientation, however, is more complex than a simple set of apertures so automatic alignment has not been as useful so far. Alignment of the capillary with the X-ray beam is accomplished by examining the far-field beam profile. The focused beam reflecting from the inner capillary surface is intrinsically more divergent than the undeflected direct beam going through the center of the optic. When viewed at long detector distances, a distinctive annular pattern emerges (Fig. 5*a*). A specially constructed beam-profile visualization camera has been designed to view the far-field beam profile. The far-field camera is mounted magnetically to the protective 'garage door' shield that normally covers the CCD detector when users are not taking exposures. A miniature monochrome

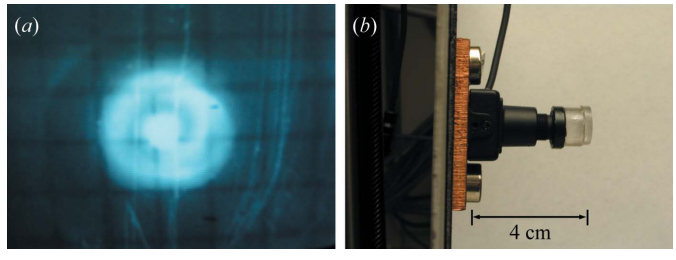

Figure 5
Far-field beam profile image and visualization camera. At large distances (>500 mm) from the capillary tip, the X-ray microbeam is annular in form as seen by fluorescence on a $CdWO_4$ crystal (*a*). The direct unfocused beam is the disc at the center while the focused beam has diverged into a halo. Black grid lines mark 1 mm squares. A mini video camera equipped with optical spacers and $CdWO_4$ crystal is fixed to the protective 'garage door' shield on the crystallography CCD detector and can be easily moved into place to check the alignment of the X-ray optic (*b*).

NTSC video camera (Super Circuits, Austin, TX, USA; part number PC180XS) has been fitted with a 6 mm clear optical spacer that holds a 10 mm × 10 mm single-crystal scintillator of $CdWO_4$ cleaved to a thickness of 0.25 mm (Saint Gobain Crystals and Detectors India Limited, Bangalore, India) and backed with a 1 mm grid for a size reference (Fig. 5*b*). The $CdWO_4$ crystals appear to be very radiation resistant, with no sign of photobleaching over time. For a capillary optic producing a 2 mrad beam divergence, the far-field beam profile can be viewed between 500 and 900 mm downstream from the capillary optic.

For alignment of the monocapillary optic to proceed, some of the X-ray beam must be initially visible in the profile camera. For the optic considered in this paper, aligning the 40 µm internal diameter occasionally presents a challenge. In such cases, we have found it helpful to first align the optical table to the X-ray beam using a capillary of larger internal diameter (>100 µm). Alignment is accomplished by alternately adjusting the rotations and translations until a fully symmetrical annular far-field pattern is visible. Highly misaligned monocapillary optics can produce asymmetric double-bounce patterns, which appear as much larger diameter crescent shapes with no direct beam spot. In such cases, the object is first to recover the direct (undeflected) beam through the center of the optic and then to work towards a symmetric pattern. Periodically throughout the run, alignment can be easily checked by moving the far-field camera into place and translating the sample and beamstop slightly out of the beam path (but still within the cold stream). The most likely cause of beam misalignment during a run is user contact to the monocapillary housing during sample mounting, though in our experience this tends not to produce any serious degradation of focus or loss of flux. In practice, profile checks and minor realignments are performed approximately every 8 h.

Alignment of the beam with the goniometer rotation φ-axis is accomplished by using scintillating glass microfibers mounted on standard crystallography bases. Terbium-doped borosilicate glass 'first draw' fibers 700 µm in diameter (LKH6 glass courtesy of Collimated Holes Inc., Campbell, CA, USA) can be easily drawn to <20 µm diameters using standard micropipette drawing technology (Narishige Scientific Instrument, Tokoyo, Japan). As in the case of $CdWO_4$ crystals, the clarity of the glass results in sharp beam profile images. Some photobleaching of the glass has been observed over time, so it is important to use a fresh segment of fiber when assessing profiles. Smaller-diameter fibers offer more accuracy in alignment at the expense of brightness, but larger-diameter fibers can be used quite effectively to assess focus quality (Fig. 6). The circle in the figure is 100 µm in diameter with 10 µm tick marks. The unfocused beam going directly through the optic is the fainter 40 µm segment, while the peak of the focused beam is visible as a bright spot at the center. Scintillating glass microfibers provide a highly accurate means of centering the rotational axis in the beam in both on-axis and off-axis microscope configurations. For thinner fibers, distortion owing to the cold stream flow can displace the apparent center of rotation by a small amount, so some care is required for high-precision alignment. In principle, fluorescence-based beam centering methods should be possible at nanometer scales.

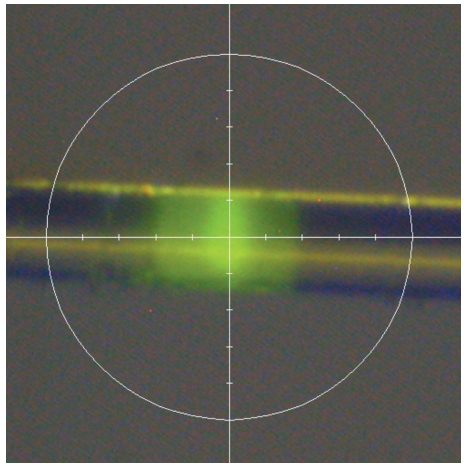

Figure 6
Terbium-doped glass fiber for aligning the sample spindle with the X-ray microbeam. X-ray-sensitive scintillating glass is easily drawn into fibers of diameter 30 µm or smaller. A cross-hair is also shown in the figure with tick marks every 10 µm. The broad green glow has a 40 µm base corresponding to the exit diameter of the capillary tip, and the focused radiation is visible as a bright spot at the center.

Special thanks to Sohyun Kim for preparing the microcrystal samples used in this work and to the staff of MacCHESS. The web-based capillary design program *ImageProf*, available at http://glasscalc.chess.cornell.edu/ImageProf.html, was created by Rong Huang. This research was conducted at the Cornell High Energy Synchrotron Source (CHESS), which is supported by the National Science Foundation and the National Institutes of Health/National Institute of General Medical Sciences under NSF award DMR-0225180, using the Macromolecular Diffraction at CHESS (MacCHESS) facility, which is supported by award RR-01646 from the National Institutes of Health, through its National Center for Research Resources

References

Aristov, V., Grigoriev, M., Kuznetsov, S., Shabelnikov, L., Yunkin, V., Weitkamp, T., Rau, C., Snigireva, I., Snigirev, A., Hoffmann, M. & Voges, E. (2000). *Appl. Phys. Lett.* **77**, 4058–4060.
Balaic, D. X., Nugent, K. A., Barnea, Z., Garrett, R. & Wilkins, S. W. (1995). *J. Synchrotron Rad.* **2**, 296–299.
Barrea, R. A., Huang, R., Cornaby, S., Bilderback, D. H. & Irving, T. C. (2009). *J. Synchrotron Rad.* **16**, 76–82.
Bilderback, D. H. & Fontes, E. (1997). *AIP Conf. Proc.* **417**, 147–155.
Bilderback, D. H., Thiel, D. J., Pahl, R. & Brister, K. E. (1994). *J. Synchrotron Rad.* **1**, 37–42.
Borek, D., Minor, W. & Otwinowski, Z. (2003). *Acta Cryst.* D**59**, 2031–2038.
Chen, G. J., Cerrina, F., Voss, K. F., Kim, K. H. & Brown, F. C. (1994). *Nucl. Instrum. Methods Phys. Res. A*, **347**, 407–411.
Cherezov, V., Höfer, N., Szebeny, D. M. E., Kolaj, O., Wall, J. G., Gillilan, R., Srinivasan, V., Jaroniec, C. P. & Caffrey, M. (2008). *Structure*, **16**, 1378–1388.
Cornaby, S., Smilgies, D.-M. & Bilderback, D. (2008). *Adv. X-ray Anal.* **52**.

Cornaby, S. W. (2008). PhD thesis, Cornell University, USA.
Cusack, S., Belrhali, H., Bram, A., Burghammer, M., Perrakis, A. & Riekel, C. (1998). *Nat. Struct. Biol.* **5**, 634–637.
Darwin, C. G. (1914*a*). *Philos. Mag.* **27**, 675–690.
Darwin, C. G. (1914*b*). *Philos. Mag.* **27**, 315–333.
Dauter, Z. (1999). *Acta Cryst.* D**55**, 1703–1717.
Engstrom, P. & Riekel, C. (1996). *Rev. Sci. Instrum.* **67**, 4061–4063.
Eshbach, O. W. (1975). *Handbook of Engineering Fundamentals*, prepared by a staff of specialists under the editorship of the late Ovid W. Eshbach and Mott Souders, 3rd ed. New York: Wiley.
Evans-Lutterodt, K., Ablett, J. M., Stein, A., Kao, C. C., Tennant, D. M., Klemens, F., Taylor, A., Jacobsen, C., Gammel, P. L., Huggins, H., Ustin, S., Bogart, G. & Ocola, L. (2003). *Opt. Express*, **11**, 919–926.
Feng, Y. P., Sinha, S. K., Fullerton, E. E., Siddons, D. P. & Hastings, J. B. (1995). *Appl. Phys. Lett.* **67**, 3647–3649.
French, S. & Wilson, K. (1978). *Acta Cryst.* A**34**, 517–525.
Furuta, K., Nakayama, Y., Shoji, M., Kaigawa, R., Hanamoto, K., Nakano, H. & Hosokawa, Y. (1993). *Rev. Sci. Instrum.* **64**, 135–142.
Glaeser, R., Facciotti, M., Walian, P., Rouhani, S., Holton, J., MacDowell, A., Celestre, R., Cambie, D. & Padmore, H. (2000). *Biophys. J.* **78**, 3178–3185.
Höfer, N., Kolaj, O., Li, H., Cherezov, V., Gillilan, R., Wall, J. G. & Caffrey, M. (2007). *Acta Cryst.* F**63**, 673–677.
Howell, J. A. & Horowitz, P. (1975). *Nucl. Instrum. Methods*, **125**, 225–230.
Hrmova, M., Varghese, J. N., De Gori, R., Smith, B. J., Driguez, H. & Fincher, G. B. (2001). *Structure*, **9**, 1005–1016.
Huang, R. & Bilderback, D. H. (2001). *Nucl. Instrum. Methods Phys. Res. A*, **467**, 978–981.
Huang, R. & Bilderback, D. H. (2004). *Synchrotron Radiation Instrumentation: Eight International Conference*, edited by T. Warwick, pp. 712–715. American Institute of Physics.
Huang, R. & Bilderback, D. H. (2006). *J. Synchrotron Rad.* **13**, 74–84.
Kang, H. C., Maser, J., Stephenson, G. B., Liu, C., Conley, R., Macrander, A. T. & Vogt, S. (2006). *Phys. Rev. Lett.* **96**, 127401.
Kirkpatrick, P. & Baez, A. V. (1948). *J. Opt. Soc. Am.* **38**, 766–774.
Krasnoff, S. B., Keresztes, I., Gillilan, R. E., Szebenyi, D. M. E., Donzelli, B. G. G., Churchill, A. C. L. & Gibson, D. M. (2007). *J. Nat. Prod.* **70**, 1919–1924.
Lagomarsino, S., Jark, W., DiFonzo, S., Cedola, A., Mueller, B., Engstrom, P. & Riekel, C. (1996). *J. Appl. Phys.* **79**, 4471–4473.
Li, P.-W. & Bi, R.-C. (1998). *J. Appl. Cryst.* **31**, 806–811.
Lu, C., Smith, A. M., Fuchs, R. T., Ding, F., Rajashankar, K., Henkin, T. M. & Ke, A. (2008). *Nat. Struct. Mol. Biol.* **15**, 1076–1083.
Mimura, H., Yumoto, H., Matsuyama, S., Sano, Y., Yamamura, K., Mori, Y., Yabashi, M., Nishino, Y., Tamasaku, K., Ishikawa, T. & Yamauchi, K. (2007). *Appl. Phys. Lett.* **90**, 051903.
Moukhametzianov, R., Burghammer, M., Edwards, P. C., Petitdemange, S., Popov, D., Fransen, M., McMullan, G., Schertler, G. F. X. & Riekel, C. (2008). *Acta Cryst.* D**64**, 158–166.
Otwinowski, Z. & Minor, W. (1997). *Macromol. Crystallogr.* A**276**, 307–326.
Pfeiffer, F., David, C., Burghammer, M., Riekel, C. & Salditt, T. (2002). *Science*, **297**, 230–234.
Pflugrath, J. W. (1999). *Acta Cryst.* D**55**, 1718–1725.
Riekel, C. (2004). *J. Synchrotron Rad.* **11**, 4–6.
Riekel, C., Burghammer, M. & Schertler, G. (2005). *Curr. Opin. Struct. Biol.* **15**, 556–562.
Sanishvili, R., Nagarajan, V., Yoder, D., Becker, M., Xu, S., Corcoran, S., Akey, D. L., Smith, J. L. & Fischetti, R. F. (2008). *Acta Cryst.* D**64**, 425–435.
Schmiedel, J., Blaukat, A., Li, S. Q., Knochel, T. & Ferguson, K. M. (2008). *Cancer Cell*, **13**, 365–373.
Schmitz, K. R., Liu, J. X., Li, S. L., Setty, T. G., Wood, C. S., Burd, C. G. & Ferguson, K. M. (2008). *Dev. Cell*, **14**, 523–534.
Shand, E. B. (1958). *Glass Engineering Handbook.* York, PA: Maple Press Company.
Snigirev, A., Bjeoumikhov, A., Erko, A., Snigireva, I., Grigoriev, M., Yunkin, V., Erko, M. & Bjeoumikhova, S. (2007). *J. Synchrotron Rad.* **14**, 227–228.
Snigirev, A., Kohn, V., Snigireva, I. & Lengeler, B. (1996). *Nature (London)*, **384**, 49–51.
Stern, E. A., Kalman, Z., Lewis, A. & Lieberman, K. (1988). *Appl. Opt.* **27**, 5135–5139.
Thiel, D. J. (1998). *J. Synchrotron Rad.* **5**, 820–822.
Varghese, J. N., Moritz, R. L., Lou, M. Z., van Donkelaar, A., Ji, H., Ivancic, N., Branson, K. M., Hall, N. E. & Simpson, R. J. (2002). *Proc. Natl. Acad. Sci. USA*, **99**, 15959–15964.
Vincze, L., Janssens, K., Adams, F., Rindby, A. & Engstrom, P. (1998). *Rev. Sci. Instrum.* **69**, 3494–3503.
Vincze, L. & Riekel, C. (2003). *X-ray Spectrom.* **32**, 208–214.
Wang, L., Rath, B. K., Gibson, W. M., Kimball, J. C. & MacDonald, C. A. (1996). *J. Appl. Phys.* **80**, 3628–3638.
Woolfson, M. M. (1970). *An Introduction to X-ray Crystallography*. New York: Cambridge University Press.
Yang, C., Courville, A. & Ferrara, J. D. (1999). *Acta Cryst.* **D**55, 1681–1689.
Yun, W. B., Viccaro, P. J., Lai, B. & Chrzas, J. (1992). *Rev. Sci. Instrum.* **63**, 582–585.